Research Article Vol. 32, No. 5 / 26 Feb 2024 / Optics Express 8189
Optics EXPRESS

Simultaneous sensing profiles of beam attenuation coefficient and volume scattering function at 180° using a single-photon underwater elastic-Raman lidar

MINGJIA SHANGGUAN,* ZHUOYANG LIAO, AND YIRUI GUO

State Key Laboratory of Marine Environmental Science, College of Ocean and Earth Sciences, Xiamen University, Xiamen 361102, China
*mingjia@xmu.edu.cn

Abstract: Lidar has emerged as a promising technique for vertically profiling optical parameters in water. The application of single-photon technology has enabled the development of compact oceanic lidar systems, facilitating their deployment underwater. This is crucial for conducting ocean observations that are free from interference at the air-sea interface. However, simultaneous inversion of the volume scattering function at 180° at 532 nm (β_m) and the lidar attenuation coefficient at 532 nm (K^m_{lidar}) from the elastic backscattered signals remains challenging, especially in the case of near-field signals affected by the geometric overlap factor (GOF). To address this challenge, this work proposes adding a Raman channel, obtaining Raman backscattered profiles using single-photon detection. By normalizing the elastic backscattered signals with the Raman signals, the sensitivity of the normalized signal to variations in the lidar attenuation coefficient is significantly reduced. This allows for the application of a perturbation method to invert β_m and subsequently obtain the K^m_{lidar}. Moreover, the influence of GOF and fluctuations in laser power on the inversion can be reduced. To further improve the accuracy of the inversion algorithm for stratified water bodies, an iterative algorithm is proposed. Additionally, since the optical telescope of the lidar adopts a small aperture and narrow field of view design, K^m_{lidar} tends to the beam attenuation coefficient at 532 nm (c_m). Using Monte Carlo simulation, a relationship between c_m and K^m_{lidar} is established, allowing c_m derivation from K^m_{lidar}. Finally, the feasibility of the algorithm is verified through inversion error analysis. The robustness of the lidar system and the effectiveness of the algorithm are validated through a preliminary experiment conducted in a water tank. These results demonstrate that the lidar can accurately profile optical parameters of water, contributing to the study of particulate organic carbon (POC) in the ocean.

1. Introduction

Detection of inherent optical properties (IOPs) in water bodies plays a crucial role in obtaining valuable insights into essential parameters such as turbidity, chlorophyll concentration (Chl), dissolved and suspended organic matter in the ocean. Moreover, these parameters serve as indicators of water health and ecosystem dynamics, providing valuable information for various applications such as ocean carbon cycling research, coastal zone management, aquatic ecology studies, and predictive modeling of water quality and ecological responses [1]. Therefore, it is crucial to observe their spatial and temporal distribution. For over the past two decades, passive ocean color images have provided a sustained synoptic view of the horizontal distribution of IOPs and color and biogeochemical parameters [2]. However, these measurements are limited to clear sky, day-light, high sun elevation angles, and are exponentially weighted toward the ocean surface [2]. The characteristics of lidar, such as its ability to penetrate three times deeper compared to passive ocean color observations, continuous observation capability day and night, high accuracy and sensitivity, and depth-resolved measurements, position it as a crucial complement to passive

#509596 https://doi.org/10.1364/OE.509596
Journal © 2024 Received 30 Oct 2023; revised 19 Jan 2024; accepted 29 Jan 2024; published 22 Feb 2024

Optics EXPRESS

remote sensing technologies [3]. Studies have demonstrated that the estimation accuracy of net primary productivity can be enhanced by up to 54% when utilizing depth-resolved lidar data [4]. In addition, oceanic lidar has been applied to various areas including the detection of underwater topography [5], scattering layers [6], diel vertical migration observations of marine organisms [7], fish [8], internal waves [9], bubbles [10], temperature and salinity [11].

Furthermore, by leveraging the capability of lidar to penetrate the air-water interface, lidar has been successfully utilized across various platforms including ships [12], unmanned aerial vehicles (UAVs) [13], aircraft [14], and even satellites [5]. However, the deployment of lidar underwater remains limited, despite its crucial role in accurately measuring IOPs of water without the interference caused by the air-sea interface, facilitating underwater scientific exploration, enabling maintenance of underwater equipment, and monitoring water environments in deep-water regions [15]. This limitation primarily stems from the fact that lidar systems generally utilize high-pulse-energy lasers and large-aperture telescopes to enhance the signal-to-noise ratio (SNR). However, this results in bulky laser systems with high power consumption, making underwater deployment of lidar challenging. Fortunately, the emergence of single-photon detection technology has driven the development of oceanic lidar towards miniaturization and low power consumption. By improving the detection sensitivity to the single-photon level, single-photon lidar can achieve long-range and high-precision parameter detection while being compact and low power [16]. Consequently, it has been applied in atmospheric remote sensing [17–19], distributed fiber optic sensing [20,21], shipborne lidar [22], and more recently, in underwater lidar systems [15,23–27].

However, utilizing single-photon underwater lidar for the detection of IOPs of water remains a challenging task. This is due to the fact that IOPs are typically calculated using two parameters obtained through lidar inversion, namely the volume scattering function at 180° at 532 nm (β_m) and the lidar attenuation coefficient at 532 nm (K^m_{lidar}) [28]. However, the inversion of β_m and K^m_{lidar} is not a straightforward process. One major limitation is that it faces an ill-posed mathematic problem, as it needs to infer two unknowns, namely, β_m and K^m_{lidar}, from a single measurement. Numerous attempts have been made to resolve this inherent ill-posed problem in the lidar equation. Initially, various algorithms have been proposed without changing the mechanism of elastic backscatter lidar, including the slope method [29], Klett method [30], Fernald method [31] and perturbation method [32], among others. Nevertheless, each method is based on a set of assumptions that may not be perfect, leading to certain levels of inverse error. Furthermore, the approach of incorporating a molecular channel or a Raman channel from water into the lidar system has been proposed, making the equation solvable [33]. Currently, by incorporating a molecular channel in the receiver, the high spectral-resolution lidar (HSRL) technique has been developed [4,34]. Recently, by combining the HSRL technique and a developed multiple scattering correction algorithm, the diffuse attenuation coefficient (K_d) can be estimated accurately [33]. However, the complexity of the HSRL system and its high requirements for frequency stability limit its implementation and operation to some extent.

Compared with the addition of molecular channels in the lidar receiver, incorporating Raman channels is relatively easier to implement and maintain. Hence, this study proposes the addition of Raman channels in the underwater lidar receiver. Benefiting from the high sensitivity of single-photon detection technology, the profile of the Raman backscattered signal from water can be obtained. By normalizing the elastic backscattered signals with the Raman backscattered signals, the sensitivity of the normalized signal to variations in the differential lidar attenuation coefficient is significantly reduced. This allows for the application of the perturbation method to invert β_m and subsequently obtain the K^m_{lidar} [32]. Moreover, the influence of geometric overlap factor (GOF) and laser power fluctuations on the β_m inversion process can be significantly reduced.

Optics EXPRESS

Furthermore, calculating the beam attenuation coefficient at 532 nm (c_m) as an IOP from the inverted K^m_{lidar} poses a significant challenge. This is because in most existing lidar systems, the utilization of large field of view (FOV) and large-aperture optical telescopes to enhance received energy [33], as well as the high platform height (airborne and spaceborne) resulting in a large footprint in the water [35], both contribute to a significant presence of multiple scattering components in the lidar backscattered signals. This leads to the inverted K^m_{lidar} tending towards the K_d, which represents the apparent optical properties (AOPs), rather than c_m [36]. In this work, the utilization of a small-aperture and narrow FOV telescope, combined with the small footprint of the underwater lidar, effectively suppresses multiple scattering in the backscattered signal, leading to the K^m_{lidar} providing an approximation of c_m. Therefore, the c_m profile is obtained through the K^m_{lidar} profile from the single-photon underwater lidar, and the relationship between c_m and K^m_{lidar} is established using a widely adopted semi-analytical Monte Carlo (MC) method.

The article is organized as follows. Firstly, the methodology is introduced, which includes the derivation of formulas. Next, a MC simulation is presented to establish the relationship between c_m and K^m_{lidar}. Subsequently, an error analysis of the proposed algorithm is conducted using four different Chl vertical distributions. Finally, an experiment is presented to validate the robustness and feasibility of both the algorithm and the lidar system.

2. Methodology

The backscatter profile of the elastic lidar can be expressed as follows:

$$P_m(\lambda_m, \sigma_m, z) = \frac{B_m \cdot Q_m(z)}{z^2} \cdot \beta_m(\lambda_m, z) \otimes g(\lambda_m, \sigma_m) \cdot \exp\left\{-2 \cdot \int_0^z [K^m_{lidar}(y)]dy\right\}, \quad (1)$$

where P_m represents the elastic backscattered signal at a depth of z, given when the emitting laser wavelength and the receiving wavelength (λ_m) are both 532 nm; B_m is a constant that includes lidar parameters independent of depth, such as the output laser power, quantum efficiency of the detector, and transmittance of the optical transceiver system; $Q_m(z)$ represents GOF of the elastic channel; β_m represents the volume scattering function at 180° at 532 nm; $g(\lambda_m, \sigma_m)$ represents the transmittance function of an elastic filter, which can be approximated as a Gaussian function with a center wavelength of λ_m and a bandwidth of σ_m; K^m_{lidar} represents the attenuation coefficient of the elastic lidar at 532 nm.

Furthermore, the backscatter profile of the Raman channel from water can be expressed as follows:

$$P_r(\lambda_r, \sigma_r, z) = \frac{B_r \cdot Q_r(z)}{z^2} \cdot \beta_t(\lambda_r, z) \otimes g(\lambda_r, \sigma_r) \cdot \exp\left\{-\int_0^z [K^m_{lidar}(y) + K^r_{lidar}(y)]dy\right\}, \quad (2)$$

where P_r represents the backscattered Raman signal from water at a depth of z when the emitted laser wavelength is 532 nm and the Raman wavelength (λ_r) is 650 nm; B_r is a constant that includes lidar parameters independent of depth, such as the output laser power, quantum efficiency of the detector, and transmittance of the optical transceiver system; $Q_r(z)$ represents GOF of the Raman channel. Since the Raman channel and the elastic channel share the same set of transceiver optical systems, $Q_r(z)$=$Q_m(z)$; β_t represents the volume scattering function at 180° for a wavelength of 650 nm, encompassing the volume scattering function at 180° of water Raman at 650 nm (β_r), as well as the contribution of chlorophyll fluorescence to the volume scattering function at 180° at that wavelength (β_f), i.e., $\beta_t = \beta_r + \beta_f$; $g(\lambda_r, \sigma_r)$ represents the transmittance function of the Raman filter, which can be approximated as a Gaussian function with a center wavelength of λ_r and a bandwidth of σ_r; K^r_{lidar} represents the lidar attenuation coefficient of the Raman lidar at 650 nm.

Optics EXPRESS

According to an empirical model [37], the β_r can be calculated as follows:

$$\beta_r(\lambda_r) = b_R(\lambda_m, \lambda_r) \cdot f_R(\lambda_m, \lambda_r) \cdot \tilde{\beta}_R(\pi), \tag{3}$$

where b_R represents the Raman scattering coefficient of water molecules when the emitted laser wavelength is 532 nm and the received Raman wavelength (λ_r) is 650 nm; f_R represents the Raman wavelength distribution function;$\tilde{\beta}_R(\pi)$ represents the Raman scattering phase function.

Firstly, by normalizing the elastic backscattered signal with the Raman backscattered signal, the resulting S_{mr} can be expressed as follows:

$$\begin{aligned} S_{mr}(\lambda_m, \lambda_r, z) &= \frac{B_m}{B_r} \cdot \frac{Q_m(z)}{Q_r(z)} \cdot \frac{\beta_m(\lambda_m,z)\otimes g(\lambda_m,\sigma_m)}{\beta_t(\lambda_r,z)\otimes g(\lambda_r,\sigma_r)} \cdot \exp\left\{-\int_0^z [K^m_{lidar}(y) - K^r_{lidar}(y)]dy\right\} \\ &= \frac{B_m}{B_r} \cdot \frac{\beta_m(\lambda_m,z)\otimes g(\lambda_m,\sigma_m)}{\beta_t(\lambda_r,z)\otimes g(\lambda_r,\sigma_r)} \cdot \exp\left[-\int_0^z \Delta K^{mr}_{lidar}(y)dy\right] \end{aligned}, \tag{4}$$

where ΔK^{mr}_{lidar} is the differential lidar attenuation coefficient, which is defined as the difference between K^m_{lidar} and K^r_{lidar}.

By normalizing, the variation of ΔK^{mr}_{lidar} with depth is significantly reduced, enabling the utilization of the perturbation method for measuring the β_m [32]. As a result, S_{mr} can be decomposed into two parts: the depth-dependent component and the depth-independent component:

$$\begin{aligned} S_{mr}(\lambda_m, \lambda_r, z) = \frac{B_m}{B_r} \cdot \frac{[\beta_m(\lambda_m,z_0)+\beta'_m(\lambda_m,z)]\otimes g(\lambda_m,\sigma_m)}{[\beta_t(\lambda_r,z_0)+\beta'_t(\lambda_r,z)]\otimes g(\lambda_r,\sigma_r)} \\ \cdot \exp\left[-\Delta K^{mr0}_{lidar} \cdot z - \int_0^z \Delta K^{mr'}_{lidar}(y)dy\right] \end{aligned}, \tag{5}$$

where β_m (λ_m, z_0), β_t (λ_r, z_0), and ΔK^{mr0}_{lidar} respectively represent the components of β_m, β_t and ΔK^{mr}_{lidar} that do not vary with depth; $\beta'_m(\lambda_m, z)$, $\beta'_t(\lambda_r, z)$ and $\Delta K^{mr'}_{lidar}$ represent the components of β_m, β_t and ΔK^{mr}_{lidar} that do vary with depth; z_0 is the depth of the first point of the measured water signal.

When the depth-dependent term is ignored, the normalized signal S_{mr0} can be expressed as follows:

$$\begin{aligned} S_{mr0}(\lambda_m, \lambda_r, z) &= \frac{B_m}{B_r} \cdot \frac{\beta_m(\lambda_m, z_0) \otimes g(\lambda_m, \sigma_m)}{\beta_t(\lambda_r, z_0) \otimes g(\lambda_r, \sigma_r)} \exp\left(-\Delta K^{mr0}_{lidar} \cdot z\right) \\ &= \frac{S_{mr}(\lambda_m, \lambda_r, z_0)}{\exp\left(-\Delta K^{mr0}_{lidar} \cdot z_0\right)} \cdot \exp\left(-\Delta K^{mr0}_{lidar} z\right) \end{aligned} \tag{6}$$

Then, after determining the ratio B_m /B_r through experimental calibration, the value of $\beta_m \otimes g$ (λ_m, σ_m) / $\beta_t \otimes g$ (λ_r, σ_r) can be expressed based on Eq. (6) as follows:

$$\frac{\beta_m(\lambda_m, z_0) \otimes g(\lambda_m, \sigma_m)}{\beta_t(\lambda_r, z_0) \otimes g(\lambda_r, \sigma_r)} = \frac{S_{mr}(\lambda_m, \lambda_r, z_0)}{\exp(-\Delta K^{mr0}_{lidar} \cdot z_0)} \cdot \frac{B_r}{B_m}. \tag{7}$$

Subsequently, the lidar attenuation coefficients in the elastic channel and Raman channels are calculated using the slope method [29], represented as $2K^m_{lidar}$ and K^m_{lidar} +K^r_{lidar} (defined as K^{mr}_{lidar}), respectively [29]. The difference between these two coefficients, denoted as K^m_{lidar} - K^r_{lidar} , is used as the initial value for ΔK^{mr0}_{lidar}.

According to the perturbation method [32], assuming $\Delta K^{mr'}_{lidar}$= 0, β_m can be expressed as follows based on Eq. (5) and Eq. (6):

$$\begin{aligned} \beta_m(\lambda_m, z) \otimes g(\lambda_m, \sigma_m) &= \frac{\beta_t(\lambda_r,z)\otimes g(\lambda_r,\sigma_r)}{\beta_t(\lambda_r,z_0)\otimes g(\lambda_r,\sigma_r)} \cdot \beta_m(\lambda_m, z_0) \otimes g(\lambda_m, \sigma_m) \cdot \frac{S_{mr}(\lambda_m,\lambda_r,z)}{S_{mr0}(\lambda_m,\lambda_r,z)} \\ &= \beta_t(\lambda_r, z) \otimes g(\lambda_r, \sigma_r) \cdot \frac{S_{mr}(\lambda_m,\lambda_r,z_0)}{\exp(-\Delta K^{mr0}_{lidar} \cdot z_0)} \cdot \frac{B_r}{B_m} \cdot \frac{S_{mr}(\lambda_m,\lambda_r,z)}{S_{mr0}(\lambda_m,\lambda_r,z)} \end{aligned}. \tag{8}$$

Optics EXPRESS

Finally, by deconvolving $g(\lambda_m, \sigma_m)$ from Eq. (8), the expression for β_m can be obtained as follows:

$$\beta_m(\lambda_m, z) = \mathcal{F}^{-1}\left\{\frac{\mathcal{F}\left[\beta_t(\lambda_r, z) \otimes g(\lambda_r, \sigma_r) \cdot \frac{S_{mr}(\lambda_m, \lambda_r, z_0)}{\exp(-\Delta K_{lidar}^{mr0} \cdot z_0)} \cdot \frac{B_r}{B_m}\right]}{\mathcal{F}[g(\lambda_m, \sigma_m)]}\right\} \cdot \frac{S_{mr}(\lambda_m, \lambda_r, z)}{S_{mr0}(\lambda_m, \lambda_r, z)}, \quad (9)$$

where $\mathcal{F}$ and $\mathcal{F}^{-1}$ respectively represent the Fourier transform and the inverse Fourier transform.

Define the coefficient $\beta_{m0}^*(\sigma_m, \sigma_r, z)$ as

$$\beta_{m0}^*(\sigma_m, \sigma_r, z) = \mathcal{F}^{-1}\left\{\frac{\mathcal{F}\left[\frac{\beta_t(\lambda_r, z) \otimes g(\lambda_r, \sigma_r) \cdot S_{mr}(\lambda_m, \lambda_r, z_0)}{\exp(-\Delta K_{lidar}^{mr0} \cdot z_0)} \cdot \frac{B_r}{B_m}\right]}{\mathcal{F}[g(\lambda_m, \sigma_m)]}\right\}. \quad (10)$$

Note that, according to our previous research [26], when the bandwidth of the Raman filter is 6 nm, $\beta_t(\lambda_r, z)$ and $\beta_r(\lambda_r)$ are essentially equal, and $\beta_r(\lambda_r)$ is depth-independent, obtainable through Eq. (3). By utilizing calibrated system constants B_r and B_m, β_{m0}^* can be calculated using Eq. (10).

Then, the inversion result can be expressed as follows:

$$\beta_m(\lambda_m, z) = \beta_{m0}^*(\sigma_m, \sigma_r, z) \cdot \frac{S_{mr}(\lambda_m, \lambda_r, z)}{S_{mr0}(\lambda_m, \lambda_r, z)}. \quad (11)$$

Then, the K_{lidar}^m can be further obtained based on Eq. (1) using β_m after calibrating the GOF of the elastic backscattered signal. The K_{lidar}^m can be expressed as follows:

$$K_{lidar}^m(z) = \frac{d\{\ln[\beta_m(\lambda_m, z) \otimes g(\lambda_m, \sigma_m)] + \ln[Q_m(z)] - \ln[P_m(\lambda_m, \sigma_m, z) \cdot z^2]\}}{dz}. \quad (12)$$

Subsequently, the relationship between K_{lidar}^m and c_m established through MC simulation can be used to obtain c_m from K_{lidar}^m. However, in the perturbation method, assuming ΔK_{lidar}^{mr0} to be depth-independent leads to increased errors in β_m inversion in inhomogeneous water. Fortunately, through subsequent theoretical error analysis, it has been revealed that even in regions with significant vertical variations in Chl, the error in the inversion of K_{lidar}^m using this algorithm remains below 10%. Therefore, to improve the accuracy of β_m inversion in inhomogeneous water, an iterative approach is proposed. Firstly, the slope of the inverted K_{lidar}^m is used to determine the need for iteration. Theoretical analysis suggests that when the slope of K_{lidar}^m is less than $10^{-3}\,\mathrm{m}^{-2}$, the retrieved β_m error is within 20% and iteration is not required. Otherwise, an iterative algorithm is employed. Initially, by utilizing the depth-invariant initial value ΔK_{lidar}^{mr0}, the profiles of K_{lidar}^m are obtained through the above process. Subsequently, utilizing the relationship between ΔK_{lidar}^{mr} and K_{lidar}^m established via MC simulations, and based on the initially inverted profile of K_{lidar}^m, the depth-varying ΔK_{lidar}^{mr0} is obtained for substitution into Eq. (6). Finally, based on Eqs. (7–12), more accurate profiles of β_m and K_{lidar}^m is obtained. Through subsequent theoretical error analysis, it is found that after iteration, even in highly chlorophyll-stratified water, the error in β_m inversion is within 20% at depths up to 10 m. To provide a clearer representation of the inversion process, a flowchart is illustrated in Fig. 1.

Optics EXPRESS

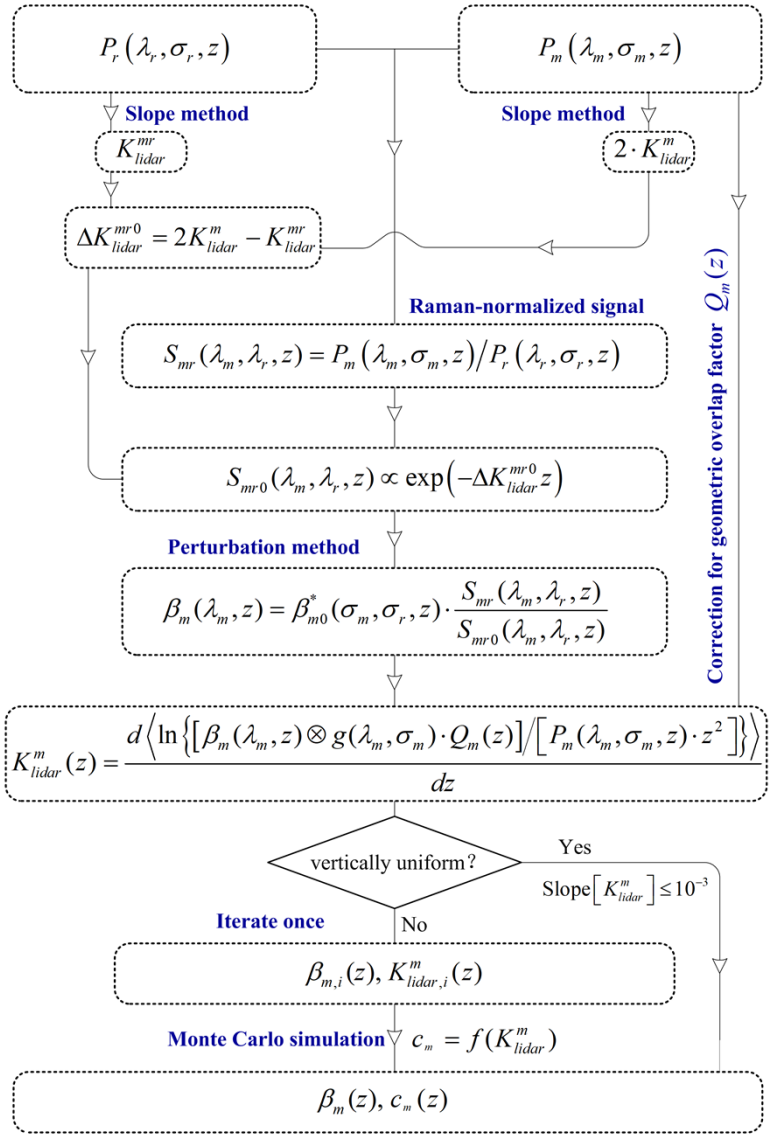

Fig. 1. Flowchart of the inversion process.

3. Relationship between c_m and K^m_{lidar}

From Section 2, it is evident that after inverting K^m_{lidar}, establishing the relationship between K^m_{lidar} and c_m is essential for further inverting c_m. This relationship is influenced not only by the hardware parameters of the lidar system but also by the IOPs of the water. To determine this relationship, this study utilizes a MC simulation, which is widely recognized as a crucial tool for simulating complex processes and has been extensively employed in simulating the backscattered signal of oceanic lidars [38]. In this study, a brief introduction to MC-based simulation of backscattered signals is provided without delving into specific details. For a more comprehensive understanding of the simulation process, it is recommended to refer to a recent article [39].

The MC method is used to simulate the random trajectories of photon propagation in a specific medium. Both the step and direction are determined by the scattering and absorption properties

Optics EXPRESS

of the medium. The step refers to the distance or interval traveled during each random sampling iteration, while the direction denotes the path taken by the photon. The MC method ignores the photon's wave properties, and the propagation of laser signal in the water is represented as the combination of many photon trajectories. The attenuation of laser energy is determined by three factors: the absorption by the medium, the scattering probability, and the probability distribution of the steps. To enhance the utilization efficiency of individual photons, a semi-analytic MC model is applied [39]. This model allows for the calculation of the expected energy value and position recording of each photon within the FOV of the telescope. The hardware parameters of the lidar used in the simulation are based on the actual single-photon underwater lidar, as shown in Table 1. The bio-optical models used in the simulation are presented in Table 2.

Table 1. Hardware parameters of the lidar system

	Parameter	Value
Pulsed laser	Radius of laser beam	2 mm
	Laser divergence angle	0.5 mrad
Coupler	Diameter of telescope	22 mm
	FOV of telescope	2.1 mrad
Scattering phase function	Petzold phase function [40]	
Other parameters	Number of photons	10^8
	Sampling interval	100 mm

Table 2. The bio-optical models used in the MC simulation

Empirical relationships	Applicable range of Chl	References
$\begin{cases} a_y(\lambda) = a_y(440)\exp[-0.014(\lambda - 440)] \\ a_y(440) = 0.2[a_w(440) + 0.06A(440)\cdot \mathrm{Chl}^{0.65}] \end{cases}$	0.02-20 mg/m^3	[41]
$b_w(\lambda) = 0.0046(450/\lambda)^{4.32}$	-	[42]
$b_R(\lambda) = 2.6\times 10^{-4}(488/\lambda)^{5.5}$	-	[37]
$b_p(\lambda) = 0.3\mathrm{Chl}^{0.62}(550/\lambda)$	0.03-30 mg/m^3	[43]

The total absorption coefficient (a) and the total scattering coefficient (b) are modeled as follows [41]:

$$a(\lambda) = a_w(\lambda) + 0.06A(\lambda)\cdot \mathrm{Chl}^{0.65} + a_y(\lambda), \tag{13}$$

$$b(\lambda) = b_w(\lambda) + b_p(\lambda) \tag{14}$$

where a_w is the absorption coefficient of pure seawater [44], A is the normalized spectral absorption values of phytoplankton pigments, a_y is the absorption coefficient of yellow substance, b_w is the scattering coefficient of pure water [42], and b_p is the scattering coefficient of particulate.

In the simulations, a widely used Petzold phase function was adopted [40]. With a sampling length of 20 m and a sampling interval of 0.1 m, a total of 200 sampling points can be obtained. As shown in Fig. 2(a) and (c), the simulated elastic backscattering signal and the Raman backscattering signal decays exponentially. To mitigate the effects of multiple scattering in the lidar backscatter signal, a small-aperture telescope with a narrow FOV is employed.

As shown in Fig. 2(a) and (c), when the Chl is low, the percentage of multiple scattering (PMS), which includes secondary scattering and higher-order scattering, is low. Consequently, the lidar signal is predominantly governed by single scattering. However, as the Chl increases, the PMS increases. Afterwards, K^m_{lidar} and K^r_{lidar} at different Chl is obtained by selecting the original signal with a PMS less than 100% and using the slope method [26]. The relationship

Optics EXPRESS

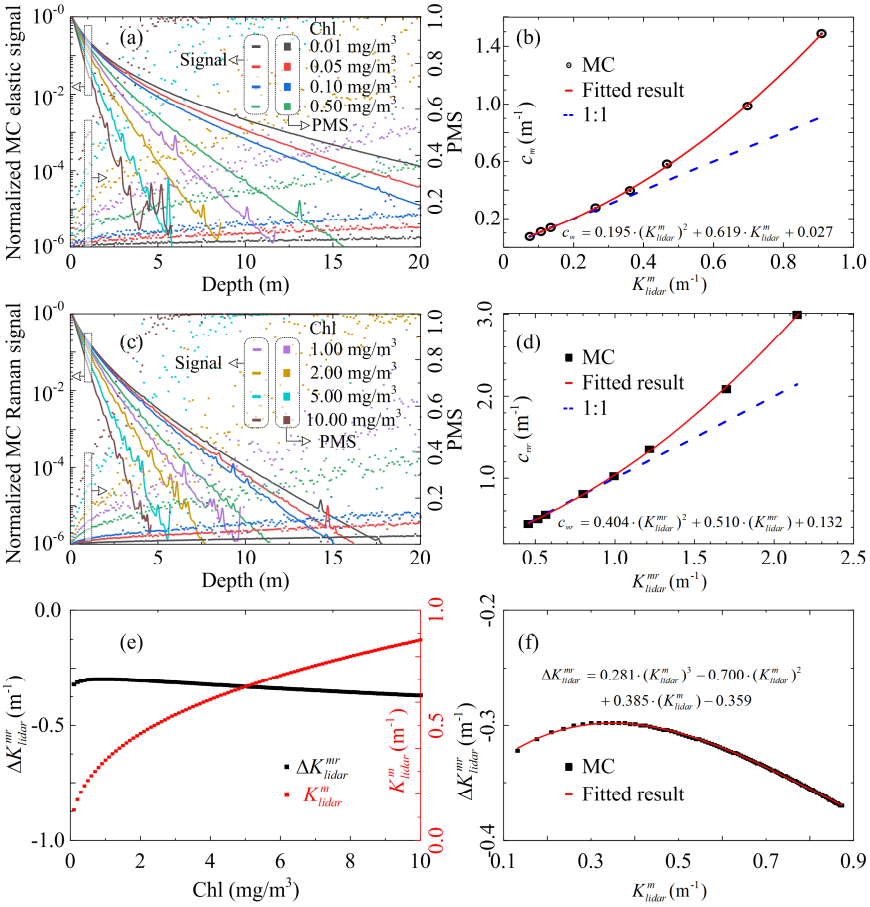

Fig. 2. (a) Simulate elastic backscattered signals (lines) and the percentage of multiple scattering (PMS) in the signals (scatters) for Chl ranging from 0.01 to 10 mg/m^3 using the Petzold phase function. (b) Relationships between K^m_{lidar} and c_m, where scatter represents the results of MC simulations, and the solid line represents the fitted results. (c) and (d) same as (a) and (b), but for Raman backscattered signals. (e) The range of ΔK^{mr}_{lidar} and K^m_{lidar} when Chl is ranging from 0.01 to 10 mg/m^3. (f) The relationship between K^m_{lidar} and ΔK^{mr}_{lidar} for Chl ranging from 0.01 to 10 mg/m^3.

between K^m_{lidar} and c_m for Chl ranging from 0.01 to 10 mg/m^3 is depicted in Fig. 2(b), while the relationship between K^{mr}_{lidar} and the sum of the beam attenuation coefficient at 532 nm and 650 nm (c_{mr}) is presented in Fig. 2(d). Subsequently, a second-order polynomial is used to fit the relationship between K^m_{lidar} and c_m for the elastic channel, as well as the relationship between K^{mr}_{lidar} and c_{mr} for the Raman channel. The fitting results are shown in Fig. 2(b) and 2(d), with a high degree of correlation indicated by the R-Square (R^2) value of 0.99 for both channels. The conclusion is consistent with the finding that K^m_{lidar} tends to closely align with the c_m when the lidar backscattered signal is predominantly governed by quasi-single scattering, whereas the lidar attenuation coefficient is given by the K_d when the backscattered signal is primarily influenced by multi-scattering [36]. Ultimately, the difference between K^m_{lidar} and K^r_{lidar}, referred to as ΔK^{mr}_{lidar}, is presented in Fig. 2(e) for Chl ranging from 0.01 to 10 mg/m^3. Additionally, the range of K^m_{lidar} for Chl ranging from 0.01 to 10 mg/m^3 is also depicted in Fig. 2(e). From Fig. 2(e), it can be

Optics EXPRESS

observed that the values of ΔK^{mr}_{lidar} range between -0.37 and -0.298, while the values of K^{m}_{lidar} range between 0.132 and 0.873. This demonstrates that using the Raman signal to normalize the elastic signal effectively reduces the range of ΔK^{mr}_{lidar}, meeting the applicable conditions of the perturbation method and leading to more stable inversion results. To enable the iteration mentioned in Section 2, the relationship between ΔK^{mr}_{lidar} and K^{m}_{lidar} is established and the results are presented in Fig. 2(f). It can be seen that the fitting results between ΔK^{mr}_{lidar} and K^{m}_{lidar} exhibit relative stability, with an R-Square value of 0.99.

4. Inversion error analysis

In this section, the errors caused by the inversion algorithm will be analyzed. It should be noted that this analysis exclusively focuses on the errors originating from the inversion algorithm, while excluding errors that arise from the SNR of the lidar backscattered signal. Four typical vertical distribution models of Chl will be used for analysis, representing subtropical center area, mid-latitude case 1 water, lakes, and water surrounding Europe [45–48]. The vertical distribution characteristics of these four Chl profiles are presented in Table 3 and their respective vertical profile curves are shown in Fig. 3.

To calculate the errors, the elastic backscattered signal and Raman backscattered signal received by the lidar are reconstructed. Firstly, utilizing the four vertical distribution models of Chl from Table 3, the values of c_m and c_{mr} are calculated based on the bio-optical model from Table 2 and using Eq. (13) and Eq. (14). Afterwards, referring to the relationship between c_m and K^{m}_{lidar}, c_{mr} and K^{mr}_{lidar} from Fig. 2, the vertical profile of K^{m}_{lidar} and K^{mr}_{lidar} can be obtained. In addition, β_m is calculated as follows:

$$\beta_m(\lambda_m, \mathrm{Chl}) = b_w(\lambda_m) \cdot \tilde{\beta}_w(180°) + b_p(\lambda_m, \mathrm{Chl}) \cdot \tilde{\beta}_p(180°), \tag{15}$$

where the models of b_w and b_p are shown in Table 2, and the values of $\tilde{\beta}_w(180°)$ and $\tilde{\beta}_p(180°)$ are respectively 0.114 [49] and 0.00318 [40].

Table 3. Vertical distribution model of Chl

Vertical distribution model	References
$\mathrm{Chl}(z) = 0.005z + 0.01$	[45]
$\mathrm{Chl}(z) = 0.01z + 0.1$	[46]
$\mathrm{Chl}(z) = 9.5\exp\left[\frac{-(z-2)^2}{2\cdot(2/2.355)^2}\right] + 0.5$	[47]
$\mathrm{Chl}(z) = 1.5\exp\left[\frac{-(z-3)^2}{2\cdot(2/2.355)^2}\right] + 9.5\exp\left[\frac{-(z-6)^2}{2\cdot(2/2.355)^2}\right] + 0.5$	[48]

The coefficient β_t of the Raman channel can be obtained using Eq. (3) and the following expression:

$$\beta_f(\lambda_f, z) = a_{ph}(\lambda_m, z)\Phi_C \frac{\lambda_m}{\lambda_f} h_C(\lambda_f) \frac{1}{4\pi}, \tag{16}$$

where $a_{ph}(\lambda_m, z)$ is the chlorophyll fluorescence absorption coefficient at an excitation wavelength of 532 nm; Φ_C is the quantum yield of chlorophyll fluorescence, which is affected by factors such as light, nutrients and temperature; λ_f is the fluorescence wavelength of 685 nm; h_C is the normalized emission wavelength function of chlorophyll fluorescence, which can be expressed from empirical model [49].

Given the reconstruction of K^{m}_{lidar} and β_m, as well as K^{mr}_{lidar} and β_t, along with the assumptions of B_m and B_r, and the knowledge of $Q_m(z)$ and $Q_r(z)$, P_m and P_r can be reconstructed based on Eq. (1) and Eq. (2).

After obtaining the reconstructed signal, the initial inversion is performed using the method mentioned in Section 2 to obtain β_m and K^{m}_{lidar}. Referring to the relationship between K^{m}_{lidar} and

Optics EXPRESS

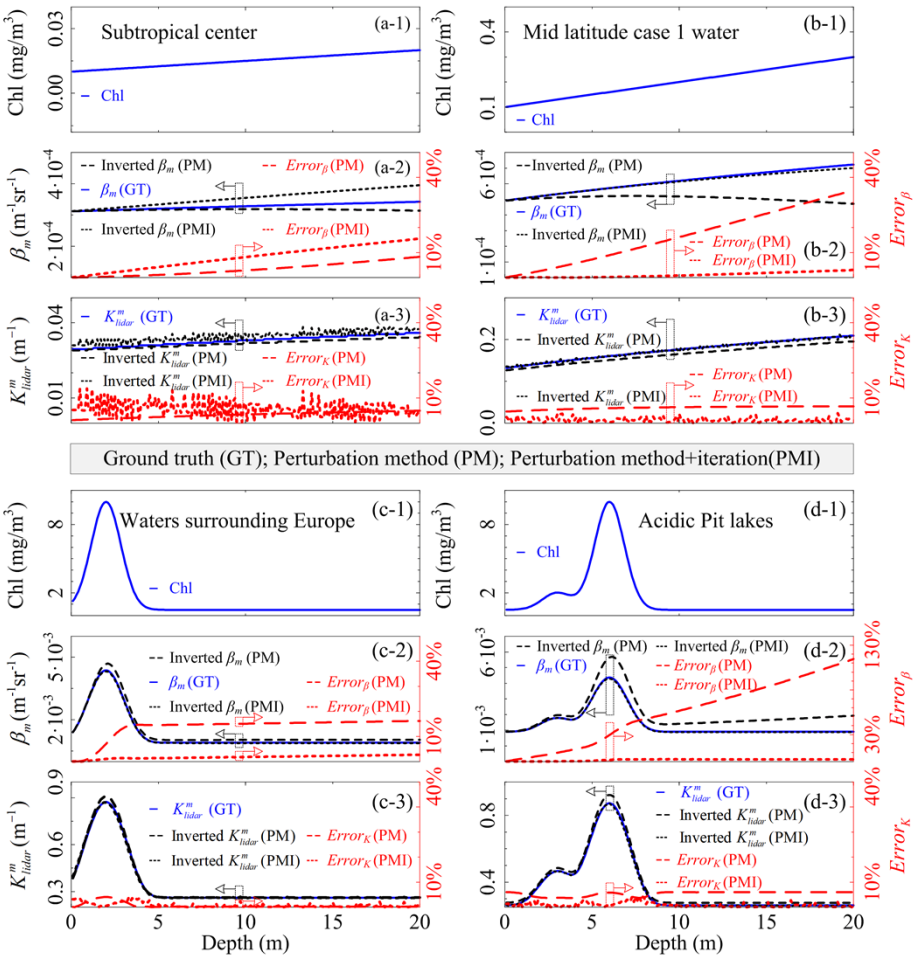

Fig. 3. Inversion errors under different vertical distributions of Chl. The sub-figures (a)-(d) show different Chl vertical distribution: (a) linearly increasing with the slope of 0.005 mg/m^{3}m^{-1} [45], (b) linearly increasing with the slope of 0.01 mg/m^{3}m^{-1} [46], (c) unimodal with a single Gaussian distribution [47], and (d) bimodal with two Gaussian distribution [48]. Each sub-figure comprises three panels. The first panel displays the corresponding Chl vertical distribution, the second panel shows the distribution of β_m and $Error_\beta$; while the third panel displays the distribution of K^m_{lidar} and $Error_K$. In the second and third panels, the blue solid line represents the true value, the sparser dotted line represents the result of the perturbation method (PM), and the denser dotted line represents the result of the perturbation method + iteration method (PMI).

ΔK^{mr}_{lidar} shown in Fig. 2(f), a new vertical distribution profile of ΔK^{mr}_{lidar} can be obtained. This new ΔK^{mr}_{lidar} is then substituted into Eq. (6) to obtain the inversion results after iteration. Finally, the respective deviations from the true values, denoted as $Error_\beta$ (error for β_m) and $Error_K$ (error for K^m_{lidar}), can be calculated as follows:

$$Error_\beta = \left| \frac{\beta_m(z) - \beta_m^{gt}(z)}{\beta_m^{gt}(z)} \right| \times 100\%, \tag{17}$$

Optics EXPRESS

$$Error_K = \left| \frac{K^m_{lidar}(z) - K^{mgt}_{lidar}(z)}{K^{mgt}_{lidar}(z)} \right| \times 100\%. \tag{18}$$

where, ${\beta^{gt}}_m$and K^{mgt}_{lidar} are the true value of β_m and K^m_{lidar} respectively.

Based on the aforementioned analysis, the $Error_\beta$and $Error_K$ for the four different Chl distributions are shown in Fig. 3. As shown in Fig. 3(a), when Chl demonstrates a linear increase with a small slope, specifically when the slope of the inverted K^m_{lidar} is less than $10^{-3}\,m^{-2}$, and the $Error_\beta$ without iteration remains below 10%, it indicates that there is no longer a need to use the iterative method. In contrast, when Chl demonstrates a linear increase with a large slope, as depicted in Fig. 3(b), the $Error_\beta$ without iteration is relatively significant, while the application of the iterative method decreases the $Error_\beta$. In the other two scenarios depicted in Fig. 3(c) and Fig. 3(d), where Chl exhibits a layered distribution ranging from 0.01 to 10 mg/m^3, the $Error_\beta$ can also be significantly reduced after iteration. These findings suggest that the iterative method is more effective in stratified waters. Conversely, in homogeneous waters, the perturbation method is sufficient for accurate inversion. Furthermore, the $Error_K$ remains below 10%, which further supports the use of iterative methods.

5. Field experiment

5.1. Lidar system

As shown in Fig. 4, the single-photon underwater lidar system includes four subsystems: a 532 nm pulsed laser, a transceiver, an optical receiver, and a data acquisition system. The system employs a compact fiber-based laser that utilizes a master oscillator power amplifier (MOPA) architecture, incorporating a single-mode pulsed seed laser operating at 1064 nm. The seed laser is amplified through a single-mode ytterbium-doped fiber amplifier (SM-YDFA) and a high-power ytterbium-doped fiber amplifier (HP-YDFA). It then passes through a lithium borate crystal (LBO) for second harmonic generation, achieving an average power output of up to 1.0 W at a wavelength of 532 nm, with a beam divergence of 0.5 mrad. The output pulse width of the laser is 501 ps, and it operates at a repetition frequency of 1 MHz.

To achieve a miniaturized and robust structure, a fiber-connected configuration is specifically designed for the underwater lidar system. The backscattered signal from water is coupled into a 105 μm multimode fiber (MMF) with a numerical aperture (NA) of 0.22. This coupling is achieved through an achromatic collimator with a 50.8 mm focal length, resulting in a narrow FOV of ~ 2.1 mrad. This narrow FOV not only provides significant suppression of noise but also suppresses multi-scattering components in the backscattered signal. The distance between the transmitted laser and the received collimator is ~20 mm.

The backscattered photons are first separated into the elastic channel and the Raman channel by DM_2. The elastic signal passes through DM_2, while the Raman signal is reflected by DM_2. Subsequently, the elastic backscattered signal is filtered using a 0.1 nm bandwidth filter ($Filter_1$) to remove background noise, while the Raman backscattered signal is extracted using a 6 nm bandwidth filter ($Filter_2$) at 650 nm. The bandwidth selection of the Raman filter is optimized to minimize the impact of laser-induced fluorescence on inversion while ensuring a sufficient SNR. For more details, please refer to a recent article [26]. The optical transmission efficiency of the elastic channel from the collimator to the detector is ~ 76%. On the other hand, the Raman channel achieves an isolation of 55 dB for the elastic backscattered signal, with a transmission efficiency of around 55%. For both channels, given the total MMF length does not exceed 1 m, the transmission efficiency of backscattered signals at 650 nm and 532 nm within the fiber surpasses 90%, corresponding to a loss of less than 0.5 dB. The elastic backscattered signal and Raman backscattered signal are then detected separately using single-photon avalanche diodes (SPADs). This single-photon detector has a detection efficiency, defined as the ratio of successfully detected photon events to the total photon count, of 62% at 650 nm and 50%

Optics EXPRESS

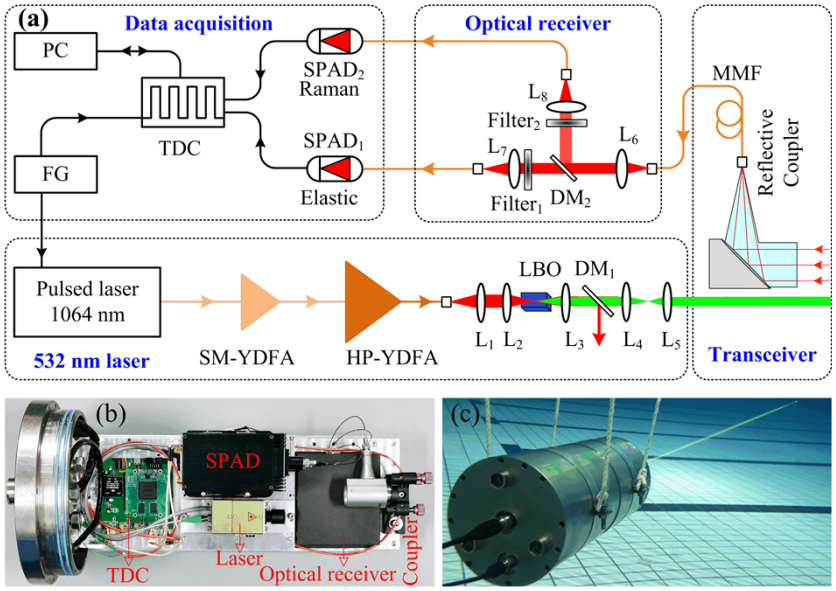

Fig. 4. (a) Optical layout of the single-photon underwater lidar. SM-YDFA: Single-Mode Ytterbium-Doped Fiber Amplifier; HP-YDFA: High-Power Ytterbium-Doped Fiber Amplifier; L: lens; LBO: lithium borate; DM: dichroic mirror; MMF: Multimode fiber; SPAD: single-photon avalanche diode; TDC: time-to-digital converter; FG: function generator; PC: personal computer. (b) Internal photo of the single-photon underwater lidar. (c) Photo of single-photon lidar in operation underwater.

at 532 nm, with a dark count rate of 50 counts per second (cps). Moreover, a self-developed two-channel time-to-digital converter (TDC) with a resolution of 500 ps is employed to accurately acquire the timing information of the backscattered photons. The electronic module utilizes a self-constructed function generator (FG) implemented on a field programmable gate array (FPGA) to generate precise control signals for the laser and TDC. The lidar features dimensions of 20 cm in diameter and 40 cm in length. With an average power consumption of approximately 80 W, the lidar has a weight of 15 kg. A summary of the system parameters is presented in Table 4.

Table 4. Key parameters of the elastic-Raman lidar system

	Parameter	Value
Pulsed laser	Wavelength	532 nm
	Pulse duration	501 ps
	Average power	1 W
	Pulse repetition rate	1 MHz
	Pulsed energy	1 μJ
Collimator	Focal length	50.8 mm
	Mode-field diameter of the MMF	105 μm
SPAD	Detection efficiency at 532 nm	50%
	Detection efficiency at 650 nm	62%
	Dark count rate	50 cps

Optics EXPRESS

5.2. Water tank experiment

To verify the stability of the single-photon underwater lidar system and the effectiveness of the inversion algorithm, a water tank experiment was carried out in a swimming pool at the Xiang'an campus of Xiamen University (24°37′N, 118°18′E). The size of the pool is 50×25×2 m^3.

In the water tank experiment, the entire single-photon lidar system was placed underwater at a depth of 1 m below the water surface. Due to the relatively wide bandwidth of the Raman filter (6 nm), the experiment was conducted in a dark environment. The raw data of P_m and P_r are shown in Fig. 5(a) with an accumulation time of 20 s. From the raw data, it can be observed that, by utilizing single-photon detection technology, the detection depth of even the Raman backscattered signals reaches ~ 20 m. Additionally, as described below, both profiles within the first 7 m do not follow an exponential decay trend due to the effect of the GOF. However, after 7 m, when the GOF is fully overlapped, the backscattered signals of the lidar exhibit an exponential decay trend. Due to the uniform mixing of water in the tank and the measurements being conducted under non-flowing conditions, the GOF can be calculated based on the elastic backscattered profile, as indicated by the black squares in Fig. 5(a). Specifically, the slope method was initially employed to calculate the value of K^m_{lidar} using the measured elastic backscattered signals beyond a distance of 7 m. By utilizing the calculated K^m_{lidar}, the signal within the range of 0-7 m can be estimated assuming a GOF of 1. Ultimately, the GOF was determined by dividing the measured elastic backscattered signals by the estimated elastic backscattered signals derived from the calculated K^m_{lidar}. By fitting the calculated GOF using a logistic function, the results are depicted by the red line in Fig. 5(a), demonstrating a high level of fit with an R^2 value of 0.99. The measured elastic backscattered signal can be corrected using the fitted GOF, as shown by the blue solid line in Fig. 5(a). Moreover, with the introduction of the GOF, a significant improvement in the dynamic measurement range of the lidar is realized. The GOF-corrected elastic backscattered signals demonstrate that the single-photon lidar achieves a dynamic measurement range exceeding 50 dB.

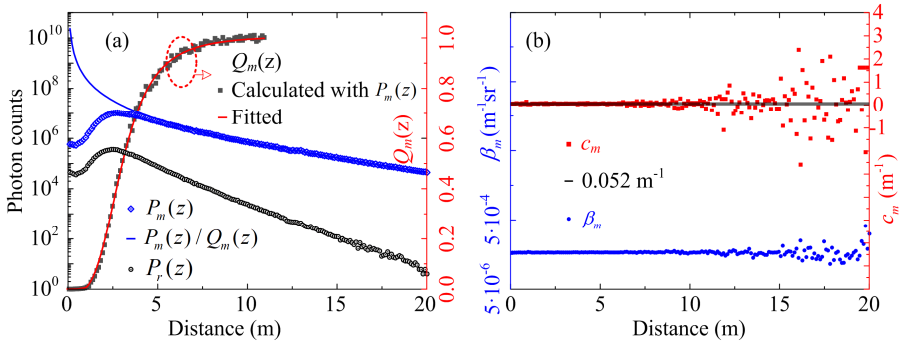

Fig. 5. Field experiment results: (a) Measured elastic backscattered signal (blue circles) and Raman backscattered signal (black circles), along with the corrected elastic backscattered signal accounting for GOF (blue solid line). The measured GOF is represented by squares, and the fitted GOF is depicted by the red line. (b) The retrieved values of β_m (blue circles) and c_m (red squares), along with the measured c_m (black solid line).

The inversion results of β_m and c_m, obtained through the inversion algorithm described in Section 2, are shown as blue circles and red squares in Fig. 5(b), respectively. During the inversion process, the value of ΔK^{mr0}_{lidar} is derived by utilizing the K^m_{lidar} and K^{mr}_{lidar}, which are determined using the slope method with the backscattered signal after 7 m. The value of B_m/B_r is obtained through calibration, which involves attenuating a broadband continuous light source

Optics EXPRESS

with a known spectral distribution to the single-photon level and coupling it into the optical collimator of the lidar system. The ratio of the elastic and Raman channel detection signals is then measured to calibrate B_m/B_r. From the figure, it can be seen that the β_m values and c_m values calculated through Raman normalization are relatively stable with respect to distance, but the fluctuation increases with distance due to the decrease in SNR. This relative stability of the detection results aligns with the fact that the water in the tank is uniformly mixed. The c_m at 532 nm was measured simultaneously using an in-situ absorption and attenuation meter ac-9 (WET Labs, Inc) to be 0.062 m^{-1}. The lidar inverted c_m is 0.052 m^{-1}. The agreement between the two results, with a relative deviation of 16%, validates the fact that in situations with a narrow FOV and small aperture, the measured K^m_{lidar} tends towards c_m [36].

6. Conclusion

In this study, we proposed and demonstrated an algorithm for simultaneously and accurately inverting the profiles of β_m and c_m. To the best of our knowledge, this is the first utilization of underwater single-photon lidar for the simultaneous inversion of β_m and c_m profiles.

In terms of hardware design, we improved the detection sensitivity of the underwater lidar to the single-photon level by employing single-photon detectors. This enhancement enabled the detection of elastic and even water Raman backscattered profiles using a low-pulse energy laser and a small aperture telescope. Furthermore, the telescope was designed with a narrow FOV and a small aperture to minimize the contribution of multiple scattering components in the lidar backscattered signals, thus making the inverted K^m_{lidar} tend towards c_m. Additionally, it is worth mentioning that the deployment of the lidar system underwater eliminates interference from the air-sea interface on laser transmittance, effectively removing the modulation of laser backscattered signal intensity caused by changes in interface smoothness. This capability is critical for accurately retrieving β_m based on intensity information from the lidar backscattered signals.

Regarding the algorithm for simultaneous inversion of β_m and c_m, we normalized the elastic backscattered signal using the water Raman backscattered signal. This approach significantly reduces the errors in β_m inversion caused by system instabilities, such as laser power fluctuations and unsynchronized detection efficiencies of the two detectors. Furthermore, the normalization reduces the variation of the differential lidar attenuation coefficient ΔK^{mr}_{lidar} with depth, allowing the use of a perturbation method for β_m inversion. Subsequently, by inverting K^m_{lidar} using the calculated β_m and establishing the relationship between c_m and K^m_{lidar} through MC, the vertical distribution of c_m can be inferred. To overcome the issue of large errors in β_m inversion when using the perturbation method in stratified water, we improved the method by introducing an additional iteration. Error analysis indicates that within a range of 20 m, even in stratified water, the errors in β_m and K^m_{lidar} inversion using this method are less than 10%. Finally, the robustness of the lidar system and the effectiveness of the algorithm were validated through a pool experiment.

In future work, particularly the effectiveness of this algorithm in stratified water, will be further experimentally verified, as this aspect is currently lacking in our study. Additionally, in-situ profile measurements and comparisons with ocean color measurements will be conducted to further validate and improve the relevant algorithms. Meanwhile, to minimize the influence of chlorophyll fluorescence on Raman backscattered signals, the use of shorter wavelength lasers, such as blue lasers, as transmitters will be considered. Once the impact of chlorophyll fluorescence on Raman backscattered signals is reduced, the bandwidth of the Raman filter can be increased, thereby improving the SNR of Raman backscattered signals. Furthermore, the considerably weaker water Raman signals compared to elastic scattering signals, along with the broader bandwidth of the Raman filter relative to the elastic channel, have somewhat impacted the system's depth detection and daytime performance. Consequently, we plan to integrate the

Optics EXPRESS

lidar system into an autonomous underwater vehicle (AUV) platform to enable the detection of biogeochemical parameters in water from the surface to deeper layers without being affected by solar radiation noise. In conclusion, this study demonstrates the significant potential of utilizing underwater single-photon lidar for accurately inverting β_m and c_m profiles, especially in situations where near-field signals are influenced by GOF. This innovative approach allows for the acquisition of precise and high-resolution observation data, crucial for accurately estimating primary productivity in the ocean and studying the cycling of marine biogeochemical parameters.

Funding. National Key Research and Development Program of China (2022YFB3901704); Innovation Program for Quantum Science and Technology (2021ZD0303102); Joint Funds of the National Natural Science Foundation of China (U2106210); Fujian Provincial Central Guided Local Science and Technology Development Special Project (2022L3078); MEL-RLAB Joint Fund for Marine Science & Technology Innovation.

Acknowledgment. The authors would like to thank Zhifeng Yang, Zaifa Lin, Jiaxin Sun, and Zhenwu Weng for their assistance in lidar data acquisition.

Disclosures. The authors declare no conflicts of interest.

Data availability. The data that support the findings of this study are available from the corresponding author upon reasonable request.

References

1. Z.-P. Lee, *Remote Sensing of Inherent Optical Properties: Fundamentals*, Tests of Algorithms, and Applications (International Ocean Colour Coordinating Group (IOCCG), 2006).
2. C. Jamet, A. Ibrahim, Z. Ahmad, *et al.*, "Going beyond standard ocean color observations: lidar and polarimetry," Front. Mar. Sci. **6**, 251 (2019).
3. J. H. Churnside and J. A. Shaw, "Lidar remote sensing of the aquatic environment," Appl. Opt. **59**(10), C92–C99 (2020).
4. J. A. Schulien, M. J. Behrenfeld, J. W. Hair, *et al.*, "Vertically-resolved phytoplankton carbon and net primary production from a high spectral resolution lidar," Opt. Express **25**(12), 13577–13587 (2017).
5. Y. Ma, N. Xu, Z. Liu, *et al.*, "Satellite-derived bathymetry using the ICESat-2 lidar and Sentinel-2 imagery datasets," Remote Sensing of Environment **250**, 112047 (2020).
6. J. H. Churnside and P. L. Donaghay, "Thin scattering layers observed by airborne lidar," ICES Journal of Marine Science **66**(4), 778–789 (2009).
7. M. J. Behrenfeld, P. Gaube, A. Della Penna, *et al.*, "Global satellite-observed daily vertical migrations of ocean animals," Nature **576**(7786), 257–261 (2019).
8. S. J. Pittman, B. M. Costa, and T. A. Battista, "Using lidar bathymetry and boosted regression trees to predict the diversity and abundance of fish and corals," Journal of Coastal Research **10053**, 27–38 (2009).
9. J. Churnside and L. Ostrovsky, "Lidar observation of a strongly nonlinear internal wave train in the Gulf of Alaska," International Journal of Remote Sensing **26**(1), 167–177 (2005).
10. M. Shangguan, Z. Yang, Z. Lin, *et al.*, "Compact long-range single-photon underwater lidar with high spatial-temporal resolution," IEEE Geoscience and Remote Sensing Letters (2023).
11. Y. Wang, J. Zhang, Y. Zheng, *et al.*, "Brillouin scattering spectrum for liquid detection and applications in oceanography," Opto-Electron. Adv **6**(1), 220016 (2023).
12. Q. Liu, S. Wu, B. Liu, *et al.*, "Shipborne variable-FOV, dual-wavelength, polarized ocean lidar: design and measurements in the Western Pacific," Opt. Express **30**(6), 8927–8948 (2022).
13. D. Wang, S. Xing, Y. He, *et al.*, "Evaluation of a New Lightweight UAV-Borne Topo-Bathymetric LiDAR for Shallow Water Bathymetry and Object Detection," Sensors **22**(4), 1379 (2022).
14. K. Li, Y. He, J. Ma, *et al.*, "A dual-wavelength ocean lidar for vertical profiling of oceanic backscatter and attenuation," Remote Sensing **12**(17), 2844 (2020).
15. A. Maccarone, K. Drummond, A. McCarthy, *et al.*, "Submerged single-photon LiDAR imaging sensor used for real-time 3D scene reconstruction in scattering underwater environments," Opt. Express **31**(10), 16690–16708 (2023).
16. M. Shangguan, Z. Yang, M. Shangguan, *et al.*, "Remote sensing oil in water with an all-fiber underwater single-photon Raman lidar," Appl. Opt. **62**(19), 5301–5305 (2023).
17. M. Shangguan, H. Xia, C. Wang, *et al.*, "All-fiber upconversion high spectral resolution wind lidar using a Fabry-Perot interferometer," Opt. Express **24**(17), 19322–19336 (2016).
18. M. Shangguan, H. Xia, C. Wang, *et al.*, "Dual-frequency Doppler lidar for wind detection with a superconducting nanowire single-photon detector," Optics letters **42**(18), 3541–3544 (2017).
19. C. Yu, M. Shangguan, H. Xia, *et al.*, "Fully integrated free-running InGaAs/InP single-photon detector for accurate lidar applications," Opt. Express **25**(13), 14611–14620 (2017).
20. H. Xia, M. Shangguan, G. Shentu, *et al.*, "Brillouin optical time-domain reflectometry using up-conversion single-photon detector," Optics Communications **381**, 37–42 (2016).

Optics EXPRESS

21. M. Shangguan, C. Wang, H. Xia, *et al.*, "Brillouin optical time domain reflectometry for fast detection of dynamic strain incorporating double-edge technique," Optics Communications **398**, 95–100 (2017).
22. P. Chen, Z. Mao, Z. Zhang, *et al.*, "Detecting subsurface phytoplankton layer in Qiandao Lake using shipborne lidar," Opt. Express **28**(1), 558–569 (2020).
23. A. Maccarone, A. Mccarthy, X. Ren, *et al.*, "Underwater depth imaging using time-correlated single-photon counting," Opt. Express **23**(26), 33911 (2015).
24. A. Maccarone, F. Rocca, A. Mccarthy, *et al.*, "Three-dimensional imaging of stationary and moving targets in turbid underwater environments using a single-photon detector array," Opt. Express **27**(20), 28437–28456 (2019).
25. X. Shen, W. Kong, P. Chen, *et al.*, "A shipborne photon-counting lidar for depth-resolved ocean observation," Remote Sensing **14**(14), 3351 (2022).
26. M. Shangguan, Z. Liao, Y. Guo, *et al.*, "Sensing the profile of particulate beam attenuation coefficient through a single-photon oceanic Raman lidar," Opt. Express **31**(16), 25398–25414 (2023).
27. Y. Chen, S. Guo, Y. He, *et al.*, "Simulation and Design of an Underwater Lidar System Using Non-Coaxial Optics and Multiple Detection Channels," Remote Sensing **15**(14), 3618 (2023).
28. M. J. Behrenfeld, Y. Hu, C. A. Hostetler, *et al.*, "Space-based lidar measurements of global ocean carbon stocks," Geophysical Research Letters **40**, 4355–4360 (2013).
29. J. H. Churnside, J. W. Hair, C. A. Hostetler, *et al.*, "Ocean backscatter profiling using high-spectral-resolution lidar and a perturbation retrieval," Remote Sensing **10**(12), 2003 (2018).
30. J. D. Klett, "Stable analytical inversion solution for processing lidar returns," Appl. Opt. **20**(2), 211–220 (1981).
31. F. G. Fernald, "Analysis of atmospheric lidar observations: some comments," Appl. Opt. **23**(5), 652–653 (1984).
32. J. H. Churnside and R. D. Marchbanks, "Inversion of oceanographic profiling lidars by a perturbation to a linear regression," Appl. Opt. **56**(18), 5228–5233 (2017).
33. Y. Zhou, Y. Chen, H. Zhao, *et al.*, "Shipborne oceanic high-spectral-resolution lidar for accurate estimation of seawater depth-resolved optical properties," Light: Science & Applications **11**(1), 261 (2022).
34. J. Hair, C. Hostetler, Y. Hu, *et al.*, "Combined atmospheric and ocean profiling from an airborne high spectral resolution lidar," in *EPJ Web of Conferences, (EDP Sciences*, 2016), 22001.
35. J. Yang, H. Zheng, Y. Ma, *et al.*, "Examining the consistency of lidar attenuation coefficient K lidar from ICESat-2 and diffuse attenuation coefficient K d from MODIS," IEEE Geoscience and Remote Sensing Letters (2023).
36. H. R. Gordon, "Interpretation of airborne oceanic lidar: effects of multiple scattering," Appl. Opt. **21**(16), 2996–3001 (1982).
37. J. S. Bartlett, K. J. Voss, S. Sathyendranath, *et al.*, "Raman scattering by pure water and seawater," Appl. Opt. **37**(15), 3324–3332 (1998).
38. D. J. Spence, B. R. Neimann, Helen M. Pask, *et al.*, "Monte Carlo modelling for elastic and Raman signals in oceanic LiDAR," Opt. Express **31**(8), 12339–12348 (2023).
39. S. Chen, P. Chen, L. Ding, *et al.*, "A New Semi-Analytical MC Model for Oceanic LIDAR Inelastic Signals," Remote Sensing **15**(3), 684 (2023).
40. T. J. Petzold, "Volume scattering functions for selected ocean waters," (Scripps Institution of Oceanography La Jolla Ca Visibility Lab, 1972).
41. Z. Lee and J. Tang, "The two faces of "Case-1" water," Journal of Remote Sensing (2022).
42. A. Morel, "Optical properties of pure water and pure seawater," Optical aspects of oceanography (1974).
43. A. Morel, "Optical modeling of the upper ocean in relation to its biogenous matter content (case I waters)," Journal of geophysical research: oceans **93**(C9), 10749–10768 (1988).
44. L. Prieur and S. Sathyendranath, "An optical classification of coastal and oceanic waters based on the specific spectral absorption curves of phytoplankton pigments, dissolved organic matter, and other particulate materials 1," Limnology and oceanography **26**(4), 671–689 (1981).
45. Y. Masuda, Y. Yamanaka, S. L. Smith, *et al.*, "Photoacclimation by phytoplankton determines the distribution of global subsurface chlorophyll maxima in the ocean," Commun Earth Environ **2**(1), 128 (2021).
46. C. D. Mobley and S. S. I. B. Wa, "Ecosystem Predictions with Approximate vs. Exact Light Fields," (2009).
47. H. Loisel, D. Stramski, B. G. Mitchell, *et al.*, "Comparison of the ocean inherent optical properties obtained from measurements and inverse modeling," Appl. Opt. **40**(15), 2384–2397 (2001).
48. J. Sánchez-España, C. Falagán, D. Ayala, *et al.*, "Adaptation of Coccomyxa sp. to extremely low light conditions causes deep chlorophyll and oxygen maxima in acidic pit lakes," Microorganisms **8**(8), 1218 (2020).
49. C. D. J. Mobley, "Light and water: radiative transfer in natural waters," (1994).